HHS Public Access

Author manuscript

Nat Microbiol. Author manuscript; available in PMC 2023 August 01.

Published in final edited form as:

Nat Microbiol. 2022 August ; 7(8): 1291–1300. doi:10.1038/s41564-022-01159-z.

Cryo-EM structure of an extracellular *Geobacter* OmcE cytochrome filament reveals tetraheme packing

Fengbin Wang[1,†], **Khawla Mustafa**[2,†], **Victor Suciu**[3], **Komal Joshi**[4], **Chi H. Chan**[4], **Sol Choi**[4], **Zhangli Su**[5], **Dong Si**[3], **Allon I. Hochbaum**[2,6], **Edward H. Egelman**[1], **Daniel R. Bond**[4]

[1]Department of Biochemistry and Molecular Genetics, University of Virginia School of Medicine, Charlottesville, VA 22903

[2]Department of Chemistry, University of California, Irvine, Irvine, CA 92617

[3]Division of Computing and Software Systems, University of Washington Bothell, Bothell, WA 98011

[4]Department of Plant and Microbial Biology, and BioTechnology Institute, University of Minnesota, Saint Paul, MN 55455

[5]Department of Genetics, University of Alabama at Birmingham, Birmingham, AL 35233

[6]Department of Materials Science and Engineering, Department of Molecular Biology and Biochemistry, and Department of Chemical and Biomolecular Engineering, University of California, Irvine, Irvine, CA 92617

Abstract

Electrically conductive appendages from the anaerobic bacterium *Geobacter sulfurreducens* were first observed two decades ago, with genetic and biochemical data suggesting that conductive fibres were type IV pili. Recently, an extracellular conductive filament of *G. sulfurreducens* was found to comprise polymerized c-type cytochrome OmcS subunits, not pilin subunits. Here we report that *G. sulfurreducens* also produces a second, thinner appendage comprised of cytochrome OmcE subunits and solve its structure using cryo-EM at ~ 4.3 Å resolution. OmcE and OmcS subunits have no overall sequence or structural similarities. Nevertheless, upon polymerization, both form filaments that share a conserved heme packing arrangement, in which hemes are coordinated by histidines in adjacent subunits. Unlike OmcS filaments, OmcE filaments are highly glycosylated. In extracellular fractions from *G. sulfurreducens*, we detected type IV pili comprised of PilA-N and -C chains, along with abundant B-DNA. OmcE is the second cytochrome filament characterized using structural and biophysical methods. We propose that there is a broad class of conductive bacterial appendages with conserved heme packing (rather than sequence homology) that enable long-distance electron transport to chemicals or other microbial cells.

Correspondence to: hochbaum@uci.edu, egelman@virginia.edu, dbond@umn.edu.
†These authors contributed equally

Author Contributions

K.M., K.J., C.H.C., and S.C. prepared samples. F.W. did the microscopy, image analysis and model building. V.S., Z.S., D.S. and F.W. did the analysis of the existing multi-heme structures. A.I.H., E.H.E. and D.R.B. directed the research. F.W., A.I.H., E.H.E and D.R.B. wrote the paper.

Competing Interests

The authors declare no competing interests.

Editor's summary

Structural analyses reveal that *Geobacter sulfurreducens* produces two different cytochrome filaments, comprised of either OmcS or OmcE, that share almost identical heme packing while having no recognizable sequence or structural similarity.

Introduction

Dissimilatory metal-reducing bacterial species such as *Geobacter* are capable of a highly flexible mode of anaerobic respiration, in which environmental metal oxides and insoluble electron acceptors outside of the bacterial cell serve as the sole electron acceptors. These electrogenic organisms can transmit electrons to extracellular Fe(III), Mn(IV) *, U(VI) [1], Tc(VII) [2], V(V) [3], high molecular weight humic substances[4], electrodes[5], and directly to other cells[6,7], via a complex series of redox proteins that include conductive filamentous appendages[8]. While *Geobacter spp.* are central to natural and technological processes such as metal cycling[9], subsurface remediation[10–12], waste treatment[13], and emerging energy generation applications[14–17], the identity and bioelectronic properties of the extracellular conductive biomolecules enabling these technologies remains a topic of active debate.

The multiheme *c*-type cytochromes OmcE, OmcS, and OmcZ are typically the most abundant proteins sheared from *G. sulfurreducens* cell surfaces after growth with metal oxides or electrode surfaces, and mutants lacking these cytochromes are defective in many aspects of extracellular electron transfer[18,19]. However, previous studies concluded that such cytochromes are unnecessary for *G. sulfurreducens* long-range extracellular conductivity, based on the hypothesis that *Geobacter* also possesses conductive non-heme 'nanowires'. These appendages, referred to as 'e-pili', are proposed to be built entirely from the N-terminal chain of the type IV pilin, PilA-N, and be capable of metallic-like conductivity due to electronic coupling between aromatic amino acids[20–24].

Recent findings suggest a more complex model of extracellular structures produced by *G. sulfurreducens*. Cryo-EM (cryo-electron microscopy) reconstructions at near-atomic resolution show that OmcS forms filaments containing a heme core[25,26], and these filaments are conductive[26], while scanning probe imaging and spectroscopy data suggest OmcZ polymerizes into a distinct filament[27]. The type IV pilus of *G. sulfurreducens* is a nonconductive filament found in extracellular preparations. This pilus is composed of two chains (PilA-N and PilA-C) lacking the closely spaced aromatic residues that were originally proposed to support long range electron transport in the PilA-N-only pilus model[28]. Consistent with the presence of cytochrome appendages, energy dispersive X-ray spectroscopy imaging also finds iron-rich fibers extending from *G. sulfurreducens* cells[29]. Based on these data, a more exhaustive structural analysis of extracellular conductive filaments is warranted[30]. To date, the only atomic structure of an extracellular cytochrome filament[25,26] that has been reported is for the OmcS cytochrome.

While biochemical and structural data are available for OmcS, OmcE has proven more difficult to characterize, despite evidence that it has a crucial role in extracellular respiration. *G. sulfurreducens* mutants lacking *omcE* (GSU0618) are defective in reduction of Fe(III)

oxides, Mn(IV) oxides[18], electrodes[31,32], U(VI) [33] and humic acids[34]. *G. metallireducens omcE* (Gmet_2896) mutants are also defective in Fe(III) oxide[35] and riboflavin reduction[36]. During 'direct interspecies electron transfer' (DIET), when *G. metallireducens* respires by transmitting electrons to *G. sulfurreducens*, *G. metallireducens omcE* is essential, but can be partially replaced by addition of conductive minerals[13,36–38]. Transcriptional data also points to OmcE being involved in extracellular conductivity, as *G. sulfurreducens* expression of *omcE* increases 3-fold with Fe(III) oxides, and as much as 9-fold with electrodes compared to growth with soluble electron acceptors[19,31,39]. Growth of *G. metallireducens* with Fe(III) oxides also upregulates *omcE* 4.4-fold[35], and in the absence of an abiotic conductive medium to aid direct electron transfer to *G. sulfurreducens*, *G. metallireducens omcE* expression increases 9-fold[38].

The study of extracellular filaments, and their roles, in *Geobacter* spp. is challenging owing to the complex regulatory relationships between type IV pili and extracellular cytochrome production. Deletion of the *pilA-N* gene (GSU1497) or other outer membrane proteins affects which cytochromes and filaments are produced by *Geobacter*[37,40,41,42]. Mutations within *pilA-N* alter the ratios of extracellular OmcS and OmcZ, which changes the measured conductivity of extracellular filament preparations[27,43,44]. These effects suggest some cytochromes might interact with pili[28] similar to how *Francisella*[45], *Vibrio*[46], *Dichelobacter*[47], and *E. coli*[48] use a type IV pilus biogenesis system for secretion of virulence factors. Because *omcS* and *omcZ* expression is influenced by the PilS/PilR two component regulatory system and intracellular cyclic dinucleotide pools, both of which can be affected by PilA levels[23,49,50], manipulation of *pilA* or *omcS* often results in unexpected changes in extracellular cytochrome levels[23,51].

In this work, we determine the unstudied OmcE cytochrome structure by cryo-EM. We constructed *G. sulfurreducens* strains containing three different *omcS* mutations, that were intended to alter the electronic structure of heme chains within OmcS, but a serendipitous outcome was that these *omcS* mutations resulted in an enrichment of extracellular OmcE filaments.

Results

Detection of OmcE in extracellular preparations

To study the details of charge transport within OmcS filaments, we made mutations that would perturb electron transport along the heme core. We engineered three *G. sulfurreducens* strains that each expressed a different single OmcS variant altering a histidine coordinating a heme within OmcS (H357M, H41M, and H38M)[52]. Both H357 and H41 coordinate the same heme in OmcS, while H38 coordinates a different heme. After proteins were sheared from cells and recovered by ammonium sulfate precipitation as previously described[26], OmcS or OmcS-like filaments (see below) were observed as bundles and aggregates, along with a mixture of other fibers. Strikingly, after centrifugation at 8,000 g for 30 minutes and treatment with DNase I, the only structures observed using cryo-EM were thinner than OmcS and represented a previously uncharacterized cytochrome filament (Fig. 1, Supplementary Fig. 1). This suggested to us that cells were compensating for a partial or complete loss of function in OmcS by expressing a different cytochrome filament.

Cryo-EM of the OmcE filament

In order to characterize these thin filaments, we used cryo-EM (Fig. 1a), and determined the structure to 4.3 Å resolution. An averaged power spectrum from raw segments (Supplementary Fig. 2) showed a meridional layer line at ~1/(34 Å), corresponding to the rise per subunit in the filament, and another layer-line near the equator at ~1/(207 Å) corresponding to the 207 Å pitch of a 1-start helix. These observations provided the initial helical parameters used to generate a ~4.3 Å resolution reconstruction as judged by a map:map Fourier shell correlation (FSC). The model:map FSC (using the model generated below) and d_{99} give a similar resolution estimation (Supplementary Fig. 3, Supplementary Table 1). The filament differed from OmcS in size and morphology, with a rise per subunit of ~34 Å with 6.1 subunits per turn (a twist of ~59°) (Supplementary Fig. 2), compared to the 46.7 Å rise per subunit and 4.3 subunits per turn of OmcS. These filaments did not show as clear a sinusoidal morphology as OmcS filaments. Filaments were ~40 Å at their widest point, compared to the ~50 Å of OmcS, and the density map clearly showed that they contained four hemes per subunit as compared with six hemes per OmcS subunit.

OmcE fit into the cryo-EM map with a Real Space Correlation Coefficient of 0.7 (Supplementary Fig. 5). To test the hypothesis that the filament was OmcE, we used AlphaFold2 to compare predicted structures for all eight tetraheme proteins encoded in the *G. sulfurreducens* genome against the experimentally determined density map. Highly accurate protein structure prediction is now possible with AlphaFold2, even if the protein of interest has minimal sequence identity or similarity with proteins of known structure[53]. Four tetraheme cytochromes had very different folds and were excluded (Supplementary Fig. 4a,b) as being possible subunits in the filament. The remaining four cytochromes, OmcE, OmcP, GSU1787, and GSU3221, roughly matched the dimensions of the subunit in the map, and were investigated further.

Of these four cytochromes, only OmcE has eight histidine residues near the Fe densities to assemble bis-coordinated hemes (Supplementary Fig. 4), and was determined to be the correct protein with a much higher Real Space Correlation Coefficient compared to the second best fit protein, which was OmcP (0.7 vs 0.35).

Using mass spectrometry analysis, we confirmed that the thin filament was OmcE by showing that OmcE, but not OmcP, was present in the samples used to obtain the cry-EM map (Supplementary Fig. 5). Consistent with this conclusion, others have reported transcriptional data showing that *omcE* expression levels are 10-fold higher than *omcP* or GSU1787[54] under the conditions we used to obtain filaments. Further, *omcE* also had a similar operon structure to the nanowire *omcS*, with an NHL-domain protein upstream of the cytochrome and no lipoproteins or accessory cytochromes to suggest it was part of an integral membrane porin-cytochrome complex[18,55]. GSU1787 and GSU3221 cytochromes were detected in our mass spectroscopy data, which suggests that they either exist in a non-filamentous form in the isolates, or that they form filaments that are of far lower abundance and therefore remain undetected in the cryo-EM image analyses.

Sequence and structural comparison of OmcE and OmcS

As OmcE filaments are only the second experimentally-determined cytochrome appendage atomic structure, our next question was whether OmcE shared any sequence or structural homology with OmcS. At the sequence level, OmcE had no detectable homology to OmcS, with ~10% sequence identity (Supplementary Fig. 6). Alignment of their cryo-EM 3D structures also suggested no similarities in the fold, although both proteins are mainly composed of random coil domains (OmcE has ~ 3% of residues in β-strands and ~17% in helices, leaving ~80% in coils and turns).The hemes in OmcE are bis-His coordinated, as are those in OmcS (Fig. 1c–d). The minimum edge-to-edge distances between hemes are also similar, ranging from 3.5–4.0 Å, suggesting similar electron transport behaviors in OmcE and OmcS filaments, and both structures have one interfacial heme per subunit coordinated by histidine ligands from an adjacent subunit.

Closer inspection of the quasi-one-dimensional arrangement of the heme chains along the filament core in OmcE and OmcS filaments revealed a further similarity. Despite the lack of overall backbone structural homology between the two proteins, the positions of the four hemes in OmcE, as well as their coordinating histidines, aligned with the first four hemes of OmcS (Fig. 2c). While the sequence similarity between both cytochromes was low, 28 atom pairs could be aligned between OmcE (200 residues) and OmcS (406 residues) with an RMSD ~1.1 Å. When comparing atom pairs across most of the OmcE model, the RMSD rose to 19 Å between 185 atom pairs (Fig. 2a,b). The four CxxCH heme-binding motifs and the additional distal histidines coordinating the hemes accounted for almost all of the residues in the 28 C_α pairs that could be aligned with a 1.1 Å RMSD between OmcE and OmcS. To the best of our knowledge, the coordination of a heme in one subunit by a histidine in an adjacent subunit in both the OmcE and OmcS filaments seems to be unique among all *c*-type cytochrome structures solved to date. The conservation of heme arrangements between OmcS and OmcE raises the possibility that the hemes are dictating the protein fold, rather than the protein determining the position of the hemes. This would be consistent with the exquisite conservation of heme arrangements, despite a lack of any sequence or structural homology between OmcS and OmcE.

There was one exception to the conserved three-dimensional histidine alignment: OmcE-H58 was structurally aligned in three dimensions to OmcS-H41 at heme 2, where they each coordinated hemes of the adjacent protein subunit (Fig. 2d). However, in a sequence-based alignment (Supplementary Fig. 6a), OmcE-H58 aligned to OmcS-H172. This was due to the backbone positions of OmcE-H58 and OmcS-H172 being close, but their side-chain conformations diverging to coordinate the next monomer's heme 2^{+1} in OmcE and heme 6 in OmcS, respectively (Fig. 2d).

Stacking arrangement of heme pairs

Given how well the four hemes could be superimposed between OmcE and OmcS, we asked whether this represented a preferred heme-heme pairing motif used in proteins capable of efficient electron transfer. For example, closely related redox partners, such as cytochrome c554 and hydroxylamine oxidoreductase (HAO), have conserved tetra-heme cores with structural similarities[56]. Similarly, chains of heme have a similar arrangements

in multiheme proteins involved in conversion of nitrogen and sulfur compounds, despite substantial divergence in overall protein structures and sequences[57].

To compare OmcE heme orientations to heme *c* pairs available in the Protein Data Bank (PDB), we looked at all 853 entries that contain heme *c* (HEC) as a ligand, and kept all pairs with a minimum edge-to-edge distance less than or equal to 6 Å. We applied a 6 Å distance limit as an arbitrary cutoff, because longer distances are less efficient for electron transfer processes. We defined the rotation angle in a heme pair as the rotation required, along with a translation, to bring one heme into alignment with that of the other heme in the pair, including heme side chains (Fig. 3a). In OmcS and OmcE filaments, all heme pairs were either "parallel-stacked," i.e. at a nearly 180° angle, or rotated from each other by about 140°. When we looked at the rotation angle for the hemes in our PDB dataset and plotted these against the edge-to-edge distances between each heme *c* pair, a clear clustering pattern was observed (Fig. 3b). This suggested that there are preferred heme-heme orientations in most known multiheme structures. Most of the minimum distances fell into the 3–4 Å range, suggesting strong selection for a few key orientations at heme-heme distances supporting efficient electron transfer.

Similar to OmcE and OmcS, rotation angles of porphyrin orientations in heme *c* pairs identified from the PDB data mostly clustered near 170–180° and 110–140°, with a smaller clustering around 50–60° for more distantly spaced hemes. Interestingly, with only one exception, there were no heme-heme pairs with an angle of rotation between 0–5.50°. The exception, PDB 6BTM, was done at a resolution (3.4 Å) where the heme cannot be positioned unambiguously if prior knowledge from high resolution crystal structures has not been used.

The clustering we identified suggests that what was previously referred to in the literature as "parallel" heme pairs would be more accurately described as "anti-parallel" pairs: one heme must be rotated nearly 180° to align with the neighboring heme. Similarly, a much larger number of heme pairs were identified with a rotation angle 110–140°, compared to those is the minor cluster at a roughly complementary angle of 50–60°. The minimum edge-to-edge distances were also larger in the 50–60° cluster, suggesting an orientation preference for densely packed bis-coordinated heme pairs at obtuse angles. Notably, all of the heme pairs of OmcS and OmcE, which form cytochrome filaments, fell into the two major clusters characteristic of closely spaced hemes.

Post-translational modifications in OmcE

In OmcS filaments, two modification sites (T82 and T119) can be directly detected in the cryo-EM map (EMD-9046), even though additional densities associated with modifications are not obvious when looking at the surface of the map. Unlike OmcS, OmcE filaments have readily apparent multiple additional densities on the filament surface due to post-translational modifications, which we hypothesize are glycosylations (Supplementary Fig. 6b,c). Although we cannot determine the identity of the post-translational modifications unambiguously due to the flexibility and limited resolution of these putative glycans, potential modification sites include S83, N86, N87, N132 and T184. The presence of multiple post-translational modifications would explain discrepancies between the predicted

mass of OmcE and its behavior as a larger-than-expected protein in both SDS-PAGE electrophoresis and MALDI-TOF[18]. As sugars do not bind SDS, the decreased mass/charge ratio of glycosylated OmcE would slow migration, and addition of 5–10 sugar molecules would account for the extra ~1–2 kDa reported in MALDI[18]. Glycosylation would also be consistent with the presence of a 17-gene cluster immediately downstream of *omcE* that contains glycosyltransferases, nucleotide-sugar epimerases, and transporters commonly associated with translocation of sugars to the periplasm (Supplementary Fig. 7).

Extracellular pili and DNA in sheared preparations

Cell appendages, such as bacterial pili[58,59], typically remain in the supernatant after sample centrifugation at 8,000 g for 30 min in preparation for deposition on cryo-EM grids, but many filaments segregated to the pellet during centrifugation. In order to more completely characterize filaments produced in our experiments, we used a milder centrifugation at 5,000 g for 1 min to remove cell debris, and visualized all extracellular filaments without using DNaseI treatment. In 5,665 cryo-EM images from these preparations, four distinct filament species were observed. We classified these filaments using 2D averages (Fig. 4a,b): (1) OmcE filaments ~40 Å in diameter; (2) mutated OmcS or OmcS-like filaments ~50 Å in diameter; (3) Type IV pili ~75 Å in diameter; (4) B-DNA filaments ~25 Å in diameter.

Type IV pili were not previously observed in preparations used to determine the atomic structure of WT OmcS filaments[26], possibly due to centrifugationsteps used in that study. Type IV pili from *G. sulfurreducens*, composed of PilA-N and PilA-C chains, were previously only detected when PilA was overexpressed[28]. In our experiments, we did not overexpress PilA-N/C, but still observed these filaments. If pili are involved in OmcS maturation or secretion, it is possible that mutations in OmcS affect periplasmic incorporation of heme or retraction of PilA.

We generated a three-dimensional reconstruction of native PilA filaments with a resolution of ~4.1 Å, yielding an unambiguous tracing of both the PilA-N and PilA-C chains in the cryo-EM map (Fig. 4c, Supplementary Table 1) consistent with the previously reported structure of the overexpressed pilus[28]. The presence of PilA-N/C Type IV pili is also consistent with their high sequence coverage from mass spectrometry of the filament isolates (Supplemental Fig. 5).

Conductive bacterial appendages were previously proposed to be type IV pili comprised solely of the PilA-N chain[60], despite the lack of a power spectrum, two-dimensional averages, or three-dimensional reconstructions verifying their identity in cryo-EM or negative stain images. We analyzed previously published images of putative PilA-N filaments from Malvankar *et al.*[61] and showed that they are OmcS filaments, based upon the power spectrum observed (Supplementary Fig. 8). Models for electron conduction in putative PilA-N filaments are predicated upon the assumption of close stacking aromatic rings[24,60,62–65]. However, these models mainly rely on a 2006 study of the type IV pilus from *Neisseria gonorrhoeae* which fitted a crystal structure into a very low resolution (12.5 Å) cryo-EM reconstruction[66]. High resolution structures of bacterial type IV pili[58,59,67–69] have subsequently become available that reveal that there is a partial melting of the N-terminal helix, a feature that would prevent continuous stacking of aromatic residues in

the *Geobacter* model. Further, high resolution structures of the *Geobacter* type IV pilus, obtained using either overexpression of PilA-N and PilA-C[28] or native expression as we report here, also show a partial melting of the N-terminal helix. Based on these higher resolution structures, we conclude that there is no evidence that *Geobacter* PilA behaves differently from any other bacterial type IV pilins studied to date.

One recent study proposed that unidentified ~3 nm filaments observed in *G. sulfurreducens* cryo-EM preparations that were used to determine the larger ~ 4–5 nm OmcS structure were "presumably" composed of PilA-N[25], in seeming contradiction to the 7.5 nm PilA-N/C filament identified here and in other studies[28]. Several points call into question that proposed identification. First, electron micrographs from that study[25] were not made public, which precludes making comparisons with OmcE or DNA structures. Second, we contend that because the PilA-N chain is highly hydrophobic[70] (Supplementary Fig. 9), a filament formed from PilA-N alone would most likely be insoluble[28]. We have never observed by cryo-EM a filament composed solely of the PilA-N chain.

When DNase I was not added to our preparations, a large amount of DNA filaments were seen in all micrographs (Fig. 4a,b). 2D averages clearly show the ~36 Å pitch (Fig. 4b) expected from B-form DNA, and a ~10 Å resolution three-dimensional reconstruction was fit well with a B-DNA atomic model (Fig. 4d). Such DNA may be due to cell lysis during shearing, or secreted as a component of the extracellular matrix during biofilm formation[71]. It has not escaped our notice that this ubiquitous DNA is similar in dimensions and morphology to many of the filaments previously ascribed to be pili nanowires, and propose that DNA might contribute to limited conductivity in biofilms, the extracellular matrix, or individual filaments[72]. Future studies isolating conductive filaments should include DNase as a control measure to discount the contribution of extracellular DNA to observed properties.

Discussion

We determined the atomic structure of a previously uncharacterized cytochrome filament composed of OmcE and show that, in addition to OmcS polymers, other extracellular filaments are produced by *G. sulfurreducens*.

Although the overall protein fold, size, and helical pitch of hexaheme OmcS and tetraheme OmcE are quite different, there is a high degree of alignment of the four hemes of OmcE with the first four hemes in OmcS, as well as the corresponding CxxCH motifs that incorporate these hemes into the cytochrome. Both proteins are largely unstructured, lacking significant amounts of secondary structure, a feature consistent with many multiheme *c*-type cytochromes. However, unstructured does not mean disordered, as disordered regions of the protein would not appear in the averaged three-dimensional cryo-EM map, and the full chains of OmcS and OmcE can be traced from these maps. Mutations, insertions, and deletions in unstructured regions could thus easily occur, as long as they did not perturb the local coordination of heme groups. This decreased selective pressure on most residues could explain the high mutation rate observed within multiheme cytochrome sequences, such as between cytochromes of closely related *G. sulfurreducens* PCA and KN400 strains, where

25.8 non-synonymous changes/1000 bases were found in OmcE compared to an average of only 5.6/1000 across the rest of the proteome[73].

A lack of secondary structure content is a feature seen in other electron transporting multiheme cytochromes such as *Shewanella baltica* MtrA, in which 80% of the protein is loops[74], similar to other MtrA homologs[75]. MtrA, a decaheme cytochrome, also shares the paired-stack heme arrangement motif with OmcS and OmcE filaments, with heme pairs falling into the two major motif clusters (Fig. 3b), and it functions as a transmembrane electron conduit in *Shewanella spp*. This motif is present in other multiheme cytochromes, such as *S. oneidensis* small tetraheme cytochrome (STC/CctA) and *Escherichia coli* NrfB, both of which lack significant sequence homology with MtrA[74]. The low sequence similarity and high fidelity of heme arrangement between these proteins suggests that the heme packing is the functional feature conferring high conductivity and rapid respiration rates. Indeed, electron transfer rates in the direction of extracellular electron transfer are calculated to be similar in OmcS filaments and the MtrAB transmembrane complex[76]. Moreover, the clustering of heme pair rotation angles and edge-to-edge distances (Fig. 3b) reveals conserved arrangements of heme across all domains of life. This arrangement could be preferred for biosynthetic reasons, for example representing an optimal solution to a steric or reaction selectivity limitation on the density of heme incorporation into the apoprotein. The antiparallel orientation of heme pairs in the 110–140° and 170–180° clusters suggest such a preference for opposing thioether linkages within heme pairs. Alternatively, the arrangement could be optimal for long range electron transport and represent a selective pressure for evolution. Whether this class of multiheme cytochromes resulted from convergent or divergent evolutionary processes is unclear, but the heme structure appears highly conserved in proteins requiring fast electron transport for their function.

What is the role of the modifications observed on the exterior of the OmcE and OmcS filaments? Glycans on the surface might protect against protease cleavage, minimize damage from free radicals produced as a by-product of cytochrome peroxidase activity, or alter binding to metal oxide electron acceptors. In archaeal filaments, it has been suggested that glycosylation plays a large role in protecting these extracellular appendages in extreme environments[77]. Regardless of their function, the potential of bis-coordinated hemes should be relatively insensitive to the protein environment surrounding the heme, let alone to distant modifications such as glycosylation. We do speculate, however, that the material coating OmcE could cause artifacts during laboratory conductivity measurements, by increasing contact resistance due to increasing charge tunneling distances.

Previously, overexpression of PilA-N and PilA-C was used to produce extracellular PilA filaments[28]. We confirm here that the native PilA pilus of *G. sulfurreducens* is composed of two chains, PilA-N and PilA-C, in strains in which the only genetic changes are residues within OmcS. This PilA structure was previously proposed to form a periplasmic pseudo-pilus, possibly to aid export of cytochrome filaments[26,28]. Whatever their true function in *G. sulfurreducens*, PilA pili and cytochrome filament levels are evidently tightly linked. Mutations affecting OmcS assembly allowed easier detection of PilA pili and OmcE polymers, while *pilA-N* mutations in prior studies decreased production of OmcS polymers. Given the importance of PilA in controlling *omcS*, *omcB*, *omcAHG*, *omcOP*, and

pgcA expression via PilS/PilR-dependent and cyclic di-GMP/cyclic AMP-GMP-dependent regulatory networks[49,50,78], changes in Type IV pilin subunits should always be expected to affect electron transfer phenotypes and production of conductive appendages in *Geobacter* experiments.

The *in situ* identification of extracellular filaments from *G. sulfurreducens* has largely been based on AFM height/diameter measurements, although the size of presumptive PilA-N pili has varied in fixed (~3 nm)[8], desiccated (3–5 nm)[20], air-dried (~3 nm)[79], spin-coated (~4–6 nm)[80], solvent-evaporated (~2 nm)[70], and humidified (3–4 nm)[24] preparations on HOPG, Pt, Au, and mica. We do not think that these measurements are well-suited for identification. Negative stain TEM[81] and AFM[82] of dried samples usually does not preserve structure, as shrinkage can readily occur. Quantitative analysis in TEM has shown that the thickness can be reduced to 60% of the native value[83]. Strong adsorption to substrates combined with dehydration can severely flatten filaments, affecting height measurements in AFM. Tip-convolution artifacts are common in AFM even when measurements are done in solution[84], which impacts observed filament diameter, and AFM of dried specimens usually does not reveal internal structure or periodicities. Even during high-resolution cryo-EM of frozen/hydrated proteins, interpretation of diameter is not simple, given the contrast-transfer function and ambiguities in defining outer edges from noisy images. Accurate dimensions can instead be derived from atomic models built into high resolution cryo-EM maps for comparisons (Supplementary Fig. 12), or descriptions can be based upon more robust measures of periodicities within these filaments such as helical pitch or rise per subunit.

Having an atomic structure, the definition of diameter can still be ambiguous. The atomic structure for OmcS filaments has a diameter of 5–7.5 nm (Supplementary Fig. 10)[25,26]. In the atomic structure, while the “local” diameter of OmcS is 5.0 nm, the smallest cylinder that would include all sinusoidal undulations would have a diameter of ~ 7.5 nm (Supplementary Fig. 10). Even a value of 5.0 nm is an approximation, as OmcS does not have a smooth surface, contains hydrogen atoms that make the diameter larger, and does not consider the larger hydrodynamic radius including tightly bound waters. As an example, despite these atomic predictions of a 5–7 nm diameter, a recent paper[27] measured dried OmcS filaments by AFM to be 3.5 nm. Due to the growing diversity of extracellular filaments, each having possible diameters between 2 to 7 nm (including DNA, pili, OmcE, OmcZ, and OmcS), additional information will now be required for conclusive identification in experiments. The understanding of long-range electron transport in bacteria will likely advance when conductivity data can be reliably linked to the internal structure of the filament being analyzed. At the present time, however, the likelihood that published *G. sulfurreducens* strains produce multiple extracellular filaments, and the presence of DNA in most samples, means that measures of conductivity attributed to a specific protein need to be treated with some caution.

There are more than 75 other multiheme cytochromes in the *G. sulfurreducens* genome alone, many with an operon structure similar to OmcS, OmcE, or OmcZ. Since we now know that the helical symmetry for multi-heme cytochrome filaments appears to be determined by the arrangement of the hemes, and not by the details of the protein fold, a possibility exists that the bundles presumed to be OmcS might actually be composed

of the hexaheme cytochrome GSU2501, which was also detected in the sample by mass spectrometry (Supp. Fig. 5). This will be a question for future studies. Finding homologs or predicting if related organisms are capable of producing similar extracellular filaments is severely limited by the rapid rate of multiheme protein sequence divergence. Our work suggests that unexpected commonalities exist among these cytochromes, including conserved heme arrangements and heme-binding motifs. The early success with machine learning-based tools such as AlphaFold means that it might soon be possible to scan genomes of distant relatives or uncultivated genera for structural homologs, based on universal characteristics of this growing cytochrome nanowire family.

Materials and Methods

G. sulfurreducens mutant construction and filament preparation

Geobacter sulfurreducens PCA was obtained from the DSMZ culture collection (DSMZ 12127). *G. sulfurreducens* colonies were isolated from agar plates (1.5 %) in anoxic basal medium with acetate (20 mM) as the electron donor and fumarate (40 mM) as the electron acceptor under a H_2:CO_2:N_2 (5:20:75) atmosphere in an anaerobic workstation 500 (Don Whitley). The pH of the medium was adjusted to 6.8, buffered with 2 g/L $NaHCO_3$, and purged with N_2:CO_2 gas (80:20) passed over a heated copper column to remove trace oxygen. Liquid cultures were grown without the addition of agar. All cultures were grown at 30 °C.

The *omcS* gene was deleted using a SacB-sucrose counter-selection strategy to generate a scarless gene deletion[85]. Primers to amplify and clone the flanking regions of *omcS* used to generate the *omcS* deletion mutant is listed in Table 1. The ~1.5 kb flanking sequences of *omcS* were combined by overlap PCR and blunt-end cloned into the SacB encoding plasmid pK18mobsacB using SmaI.

The *omcS* sequences with mutations encoding the H38M, H41M and H357M variants were synthesized and cloned into the pTwist-Amp vector by Twist Biosciences (San Francisco, CA), listed in Table 2. Expression of the *omcS* mutants were under the control of a moderate (*acpP*, pTn7m) or higher expression (*ppcA* pTn7-Geo7) promoter when subcloned into either pTn7m or pTn7-Geo7 using NdeI and ApaLI. The *omcS* mutant genes were integrated 25bp downstream of the *glmS* gene in the *omcS* deletion strain using a targeted Tn7-based strategy by tri-parental mating with *Escherichia coli* conjugative donor strain MFDpir and Tn7 mobilization machinery encoded in pTns3[54,86].

For all experiments, *G. sulfurreducens* variants were revived from frozen stocks anaerobically and grown from single colony picks on 1.5% agar plates (NBFA medium) containing 20 mM acetate donor and 40 mM fumarate acceptor[87]. NBFA liquid medium is composed of 20 mM acetate donor and 40 mM fumarate acceptor, 0.38 g/L potassium chloride, 0.2 g/L ammonium chloride, 0.069 g/L monosodium phosphate, 0.04 g/L calcium chloride dihydrate, 0.2 g/L magnesium sulfate heptahydrate, 2.0 g/L sodium bicarbonate, and 10 mL mineral mix[88]. Resazurin and cysteine were omitted. NBFA media were sterilized and degassed using 80:20 N2:CO2. All chemicals were purchased from Fisher Scientific unless otherwise noted.

Cells from full-grown cultures of *G. sulfurreducens* were pelleted after reaching stationary phase via centrifugation at 4600xg for 25 min at 4 °C. Cells were re-suspended in 50 mM Tris-HCl (pH 7.5) followed by mechanical shearing to detach the extracellular filaments using Waring Commercial Blender (Cat. No. 7011S) at low speed setting for 5 min[26]. Centrifugation at 10,000xg for 15 min removed cells, and filaments were precipitated from the supernatant with 10% ammonium sulfate overnight at 4 °C while stirring, followed by centrifugation at 17,000xg for 1 hour. The final filament pellets were re-suspended in 10 mL Tris-HCl buffer. To help remove contaminants, filament samples were dialyzed with 300 kDa dialysis tubing (Biotech CE, Repligen) against ultrapure water (pH 4.3).

Gel analysis of filament samples

To separate via sodium-dodecyl sulfate - polyacrylamide gel electrophoretic (SDS-PAGE), the filament samples were mixed with reducing sample buffer with 0.3% w/v final concentration of SDS and 1.5% v/v final concentration of β-mercaptoethanol (TCI America). All samples were heated for 5 min at 100 °C and then cooled and spun at 2500xg for 1 min before loading samples into the gel. The filament samples were run on 4–16% Tricine-SDS-PAGE gels[89] prepared using Acryl/Bis (37.5:1, 40% w/v) solution (VWR) with an initial voltage of 30 V for 20 min and next voltage step of 200V for 3 hours. Spectra multicolor broad range protein ladder (ThermoFisher) was used to reference the molecular weight of the protein bands. Gels were stained both with silver stain[90] or with 3,3′,5,5′- tetramethylbenzidine (TMB)[91] after washing with ultrapure water. β-mercaptoethanol addition was omitted for Heme (TMB) stain samples.

In-Solution Tryptic Digestion

The filament samples were centrifuged at 8000×*g* for 30 min, and the supernatants were dialyzed with 300 kDa dialysis tubing against ultrapure water. Concentrator 30 kDa units (Spin-X® UF, Corning) were used to obtain > 0.2 mg/mL protein concentration and remove remnant salts and other small molecular weight contaminants. The filaments obtained after the concentration were digested in-solution using Trypsin Gold (Promega). Following the Promega protocol, a 100 μg of trypsin was resuspended in 50 mM acetic acid to reach 1 μg/μL and diluted to 20 μg/mL in a solution of 40 mM ammonium bicarbonate in 10% acetonitrile. 50 μL of the filament samples were reduced by 5 μL of 100 mM DL-dithiothreitol (Sigma-Aldrich) and the samples were heated for 5 min at 95 °C and followed by 20 min incubation at 37 °C. 20 μL of 100 mM iodoacetamide (Sigma-Aldrich) was added to all filament samples and incubated in the dark for 1 hour. Then, the reaction was diluted with 150 μL of 50 mM Tris-HCl (pH 7.5) buffer before adding 10 μL trypsin and incubating overnight at 37 °C.

Mass spectrometry of filament samples

The in-solution tryptic digestion of filament samples were quenched after overnight incubation by adding 25 μL of 5% formic acid before MALDI-TOF/TOF (UltrafleXtreme, Bruker) characterization in positive ion mode. The matrix solution was freshly made of saturated solution of α-cyano-4-hydroxycinnamic acid (Sigma-Aldrich) dissolved in a 2:1 solution of ultrapure water: acetonitrile[80]. The collected mass spectra were analyzed using mMass© protein identification software[92–94].

Cryo-EM conditions and image processing

The cell appendage sample (ca. 2–2.5 μl) was applied to glow-discharged lacey carbon grids, and then plunge frozen using an EM GP Plunge Freezer (Leica). The cryo-EMs were collected on a 300 keV Titan Krios with a K3 camera (University of Virginia) at 1.08 Å/pixel and a total dose of ca. 50 e/Å^2. Motion corrections and CTF estimations were done in cryoSPARC[95–97]. Particles were auto-picked by "Filament Tracer". All auto-picked particles were subsequently 2D classified with multiple rounds, and all particles in bad 2D averages were removed. After this, the OmcE dataset had 346,826 particles left with a shift of 35 pixels between adjacent boxes, while the PilA dataset had 112,011 particles left with a shift of 6 pixels. The possible helical symmetries were calculated from an averaged power spectrum for each filament species generated from the raw particles. For each filament species, the actual helical symmetry was then determined in cryoSPARC by trial and error until amino acid side chains and the hand of α-helices were seen[98,99]. The resolution of each reconstruction was estimated by Map:Map FSC, Model:Map FSC, and d_{99}[100]. The final volumes were then sharpened with a negative B-factor automatically estimated in cryoSPARC, and the statistics are listed in Supplementary Table 3.

Model building of PilA filaments

The density corresponding to a single PilA complex was segmented from the experimental cryo-EM density using Chimera[101]. A single PilA (PilA-N + PilA-C) from 6VK9 was used as the starting model and real-space refined in PHENIX[102]. Using the determined helical symmetry, a filament model was generated in Chimera and refined against the full cryo-EM map using PHENIX real-space refinement. MolProbity[103] was used to evaluate the quality of the filament model. The refinement statistics are shown in supplemental Table 1. The rmsd between our filament model and 6VK9 was 0.3 Å over 163 atom pairs.

Model building of OmcE filaments

The hand of the OmcE filaments was determined by the hand of an α-helix. The hand assignment also agreed with the AlphaFold2[53] models of OmcE and its three structurally-related homologs. To determine which cytochrome protein best fit into the cryo-EM map, the fit of OmcE and homologs were separately estimated and real-space refined against the map in PHENIX[102]. OmcE was the best fit with a large RCSS difference compared to the second-best fit protein OmcP (0.7 vs 0.35). To better refine heme interacting areas at this resolution, bond/angle restraints for the heme molecule itself, His-Fe, and Cys-heme thioester bonds were restricted based on the geometries obtained in high resolution crystal structures such as NrfB[104] (PDB 2P0B) and NrfHA[105] (PDB 2J7A). MolProbity[103] was used to evaluate the quality of the filament model. The refinement statistics are shown in Supplementary Table 1.

Structural analysis of heme c pairs

All structural coordinates with heme c ligand (HEC) were downloaded from the Protein Data Bank. All possible heme pairs were then filtered with a minimum distance less than or equal to 6 Å, with the "contact" command in UCSF-ChimeraX[106]. For each qualified pair, the rotation matrix between two hemes were generated in ChimeraX using the "align"

command. The rotation angle θ was then calculated from the rotation matrix with the following equation, where tr is the trace of the rotation matrix:

$$|\theta| = \arccos\left(\frac{\mathrm{tr}(R)-1}{2}\right)$$

Data Availability

The three-dimensional reconstruction for OmcE has been deposited in the Electron Microscopy Data Bank with accession code EMD-25879 (https://www.ebi.ac.uk/emdb/EMD-25879), and the atomic model has been deposited in the Protein Data Bank with accession code 7TFS (https://www.rcsb.org/structure/7tfs). The three-dimensional reconstruction for PilA-N/C has been deposited in the Electron Microscopy Data Bank with accession code EMD-25881 (https://www.ebi.ac.uk/emdb/EMD-25881), and the atomic model has been deposited in the Protein Data Bank with accession code 7TGG (https://www.rcsb.org/structure/7tgg). Other atomic models used in the study were PDB 2P0B (https://www.rcsb.org/structure/2p0b), 2J7A (https://www.rcsb.org/structure/2j7a) and 6VK9 (https://www.rcsb.org/structure/6vk9).

Supplementary Material

Refer to Web version on PubMed Central for supplementary material.

Acknowledgments

The cryo-EM imaging was done at the Molecular Electron Microscopy Core Facility at the University of Virginia, which is supported by the School of Medicine and built with NIH grant G20-RR31199. Mass spectrometry was performed in the Department of Chemistry Mass Spectrometry Facility at the University of California, Irvine on an instrument generously donated by Biosera. This work was supported by NIH Grant GM122510 (E.H.E.), K99GM138756 (F.W.), DOE grant DE-SC0020322 (A.I.H., D.R.B., E.H.E.), AFOSR grant FA9550-19-1-0380 (A.I.H), NSF grant 2030381 (D.S.), Office of Naval research grant N00014-18-1-2632 (C.H.C, K.J., and S. C.) and the SRCP Seed Grant at the University of Washington Bothell (D.S). We thank Dr. Benjamin Katz and Dr. Carrie Wilmot for helpful discussions.

REFERENCES

1. Lovley DR, Phillips EJP, Gorby YA & Landa ER Microbial reduction of uranium. Nature 350, 413–416 (1991).
2. Lloyd JR, Sole VA, Van Praagh CV & Lovley DR Direct and Fe(II)-mediated reduction of technetium by Fe(III)-reducing bacteria. Appl. Environ. Microbiol. 66, 3743–3749 (2000). [PubMed: 10966385]
3. Ortiz-Bernad I, Anderson RT, Vrionis HA & Lovley DR Vanadium respiration by *Geobacter metallireducens*: novel strategy for in situ removal of vanadium from groundwater. Appl. Environ. Microbiol. 70, 3091–3095 (2004). [PubMed: 15128571]
4. Lovley DR, Coates JD, BluntHarris EL, Phillips EJP & Woodward JC Humic substances as electron acceptors for microbial respiration. Nature 382, 445–448 (1996).
5. Bond DR, Holmes DE, Tender LM & Lovley DR Electrode-reducing microorganisms that harvest energy from marine sediments. Science (New York, NY) 295, 483–485 (2002).
6. Summers ZM et al. Direct exchange of electrons within aggregates of an evolved syntrophic coculture of anaerobic bacteria. Science (New York, NY) 330, 1413–1415 (2010).

7. Morita M et al. Potential for direct interspecies electron transfer in methanogenic wastewater digester aggregates. mBio 2(2011).
8. Reguera G et al. Extracellular electron transfer via microbial nanowires. Nature 435, 1098–1101 (2005). [PubMed: 15973408]
9. Lovley DR, Holmes DE & Nevin KP Dissimilatory Fe(III) and Mn(IV) reduction. Adv. Microb. Physiol. 49, 219–286 (2004). [PubMed: 15518832]
10. Lovley DR Bioremediation - Anaerobes to the rescue. Science (New York, NY) 293, 1444–1446 (2001).
11. Wall JD & Krumholz LR Uranium reduction. Annu. Rev. Microbiol. 60, 149–166 (2006). [PubMed: 16704344]
12. Cardenas E et al. Microbial communities in contaminated sediments, associated with bioremediation of uranium to submicromolar levels. Appl. Environ. Microbiol. 74, 3718–3729 (2008). [PubMed: 18456853]
13. Shrestha PM et al. Syntrophic growth with direct interspecies electron transfer as the primary mechanism for energy exchange. Environmental Microbiology Reports 5, 904–910 (2013). [PubMed: 24249299]
14. Cao X et al. A new method for water desalination using microbial desalination cells. Environ. Sci. Technol. 43, 7148–7152 (2009). [PubMed: 19806756]
15. Gong Y et al. Benthic microbial fuel cell as direct power source for an acoustic modem and seawater oxygen/temperature sensor system. Environ. Sci. Technol. 45, 5047–5053 (2011). [PubMed: 21545151]
16. Lovley DR et al. *Geobacter*: the microbe electric's physiology, ecology, and practical applications. Adv. Microb. Physiol. 59, 1–100 (2011). [PubMed: 22114840]
17. Rabaey K, Girguis P & Nielsen LK Metabolic and practical considerations on microbial electrosynthesis. Current Opinion in Biotechnology 22, 371–377 (2011). [PubMed: 21353525]
18. Mehta T, Coppi MV, Childers SE & Lovley DR Outer membrane c-type cytochromes required for Fe(III) and Mn(IV) oxide reduction in *Geobacter sulfurreducens*. Appl. Environ. Microbiol. 71, 8634–8641 (2005). [PubMed: 16332857]
19. Nevin KP et al. Anode biofilm transcriptomics reveals outer surface components essential for high density current production in *Geobacter sulfurreducens* fuel cells. PloS one 4, e5628 (2009). [PubMed: 19461962]
20. Malvankar NS et al. Tunable metallic-like conductivity in microbial nanowire networks. Nat. Nanotechnol. 6, 573–579 (2011). [PubMed: 21822253]
21. Malvankar NS & Lovley DR Microbial nanowires for bioenergy applications. Current Opinion in Biotechnology 27C, 88–95 (2014).
22. Wang O, Zheng S, Wang B, Wang W & Liu F Necessity of electrically conductive pili for methanogenesis with magnetite stimulation. PeerJ 6(2018).
23. Clark MM & Reguera G Biology and biotechnology of microbial pilus nanowires. Journal of Industrial Microbiology & Biotechnology 47, 897–907 (2020). [PubMed: 33009965]
24. Liu X, Walker DJF, Nonnenmann SS, Sun D & Lovley DR Direct observation of electrically conductive pili emanating from Geobacter sulfurreducens. mBio (2021).
25. Filman DJ et al. Cryo-EM reveals the structural basis of long-range electron transport in a cytochrome-based bacterial nanowire. Commun Biol 2, 219 (2019). [PubMed: 31240257]
26. Wang F et al. Structure of Microbial Nanowires Reveals Stacked Hemes that Transport Electrons over Micrometers. Cell 177, 361–369 (2019). [PubMed: 30951668]
27. Yalcin SE et al. Electric field stimulates production of highly conductive microbial OmcZ nanowires. Nature Chemical Biology 16, 1136–+ (2020). [PubMed: 32807967]
28. Gu Y et al. Structure of *Geobacter* pili reveals secretory rather than nanowire behaviour. Nature 597, 430–434 (2021). [PubMed: 34471289]
29. Lebedev N, Stroud RM, Yates MD & Tender LM Spatially resolved chemical analysis of *Geobacter sulfurreducens* cell surface. ACS Nano 13, 4834–4842 (2019). [PubMed: 30943001]

30. Yalcin SE & Malvankar NS The blind men and the filament: Understanding structures and functions of microbial nanowires. Current Opinion In Chemical Biology 59, 193–201 (2020). [PubMed: 33070100]
31. Holmes DE et al. Microarray and genetic analysis of electron transfer to electrodes in *Geobacter sulfurreducens*. Environmental microbiology 8, 1805–1815 (2006). [PubMed: 16958761]
32. Richter H et al. Cyclic voltammetry of biofilms of wild type and mutant *Geobacter sulfurreducens* on fuel cell anodes indicates possible roles of OmcB, OmcZ, type IV pili, and protons in extracellular electron transfer. Energy & Environmental Science 2, 506–516 (2009).
33. Shelobolina ES et al. Importance of c-Type cytochromes for U(VI) reduction by *Geobacter sulfurreducens*. BMC Microbiology 7, 16 (2007). [PubMed: 17346345]
34. Voordeckers JW, Kim B-C, Izallalen M & Lovley DR Role of *Geobacter sulfurreducens* outer surface c-type cytochromes in reduction of soil humic acid and anthraquinone-2,6-disulfonate. Appl. Environ. Microbiol. 76, 2371–2375 (2010). [PubMed: 20154112]
35. Smith JA, Lovley DR & Tremblay PL Outer cell surface components essential for Fe(III) oxide reduction by Geobacter metallireducens. Appl. Environ. Microbiol. 79, 901–907 (2013). [PubMed: 23183974]
36. Huang L, Liu X, Ye Y, Chen M & Zhou S Evidence for the coexistence of direct and riboflavin-mediated interspecies electron transfer in *Geobacter* co-culture. Environmental microbiology 22, 243–254 (2020). [PubMed: 31657092]
37. Liu X, Zhuo S, Rensing C & Zhou S Syntrophic growth with direct interspecies electron transfer between pili-free *Geobacter* species. The ISME Journal 12, 2142–2151 (2018). [PubMed: 29875437]
38. Zheng S, Liu F, Li M, Xiao L & Wang O Comparative transcriptomic insights into the mechanisms of electron transfer in *Geobacter* co-cultures with activated carbon and magnetite. Sci. China Life Sci. 61, 787–798 (2018). [PubMed: 29101585]
39. Aklujkar M et al. Proteins involved in electron transfer to Fe(III) and Mn(IV) oxides by *Geobacter sulfurreducens and Geobacter uraniireducens*. Microbiology (Reading, England) 159, 515–535 (2013).
40. Klimes A et al. Production of pilus-like filaments in *Geobacter sulfurreducens* in the absence of the type IV pilin protein PilA. FEMS Microbiology Letters 310, 62–68 (2010). [PubMed: 20629752]
41. Richter LV, Sandler SJ & Weis RM Two isoforms of the *Geobacter sulfurreducens* PilA have distinct roles in pilus biogenesis, cytochrome localization, extracellular electron transfer and biofilm formation. Journal of Bacteriology (2012).
42. Kim B-C et al. Insights into genes involved in electricity generation in *Geobacter sulfurreducens* via whole genome microarray analysis of the OmcF-deficient mutant. Bioelectrochemistry (Amsterdam, Netherlands) 73, 70–75 (2008).
43. Cologgi DL, Lampa-Pastirk S, Speers AM, Kelly SD & Reguera G Extracellular reduction of uranium via Geobacter conductive pili as a protective cellular mechanism. Proc. Natl. Acad. Sci. U.S.A. 108, 15248–52 (2011). [PubMed: 21896750]
44. Cologgi DL, Otwell AE, Speers AM, Rotondo JA & Reguera G Genetic analysis of electroactive biofilms. International microbiology : the official journal of the Spanish Society for Microbiology, 1–18 (2021).
45. Hager AJ et al. Type IV pili-mediated secretion modulates *Francisella* virulence. Molecular Microbiology 62, 227–237 (2006). [PubMed: 16987180]
46. Kirn TJ, Bose N & Taylor RK Secretion of a soluble colonization factor by the TCP type 4 pilus biogenesis pathway in *Vibrio cholerae*. Molecular Microbiology 49, 81–92 (2003). [PubMed: 12823812]
47. Han X et al. Twitching motility is essential for virulence in *Dichelobacter nodosus*. Journal of Bacteriology 190, 3323–3335 (2008). [PubMed: 18310333]
48. Oki H et al. Interplay of a secreted protein with type IVb pilus for efficient enterotoxigenic *Escherichia coli* colonization. Proc. Natl. Acad. Sci. U.S.A. 115, 7422–7427 (2018). [PubMed: 29941571]

49. Kilmury SLN & Burrows LL Type IV pilins regulate their own expression via direct intramembrane interactions with the sensor kinase PilS. Proc. Natl. Acad. Sci. U.S.A. 113, 6017–6022 (2016). [PubMed: 27162347]
50. Tan Z et al. The signaling pathway that cGAMP riboswitches found: analysis and application of riboswitches to study cGAMP signaling in *Geobacter sulfurreducens*. Int. J. Mol. Sci. 23, in press (2022).
51. Juarez K et al. PilR, a transcriptional regulator for pilin and other genes required for Fe(III) reduction in *Geobacter sulfurreducens*. J. Mol. Microbiol. Biotechnol. 16, 146–58 (2009). [PubMed: 18253022]
52. Hosseinzadeh P & Lu Y Design and fine-tuning redox potentials of metalloproteins involved in electron transfer in bioenergetics. Biochim Biophys Acta 1857, 557–581 (2016). [PubMed: 26301482]
53. Jumper J et al. Highly accurate protein structure prediction with AlphaFold. Nature 596, 583–589 (2021). [PubMed: 34265844]
54. Hallberg ZF et al. Structure and mechanism of a Hypr GGDEF enzyme that activates cGAMP signaling to control extracellular metal respiration. Elife 8(2019).
55. Jimenez Otero F, Chan CH & Bond DR Identification of different putative outer membrane electron conduits necessary for Fe(III) Citrate, Fe(III) Oxide, Mn(IV) Oxide, or electrode reduction by *Geobacter sulfurreducens*. J Bacteriol 200, e00347–18 (2018). [PubMed: 30038047]
56. Iverson TM et al. Heme packing motifs revealed by the crystal structure of the tetra-heme cytochrome c554 from Nitrosomonas europaea. Nat Struct Biol 5, 1005–12 (1998). [PubMed: 9808046]
57. Kartal B & Keltjens JT Anammox Biochemistry: a Tale of Heme c Proteins. Trends Biochem Sci 41, 998–1011 (2016). [PubMed: 27669648]
58. Wang F et al. Cryoelectron microscopy reconstructions of the *Pseudomonas aeruginosa* and *Neisseria gonorrhoeae* type IV pili at sub-nanometer resolution. Structure 25, 1423–1435 e4 (2017). [PubMed: 28877506]
59. Kolappan S et al. Structure of the *Neisseria meningitidis* Type IV pilus. Nat. Commun. 7, 13015 (2016). [PubMed: 27698424]
60. Lovley DR & Walker DJF Geobacter protein nanowires. Front Microbiol 10, 2078 (2019). [PubMed: 31608018]
61. Malvankar NS et al. Structural basis for metallic-like conductivity in microbial nanowires. mBio 6, e00084 (2015). [PubMed: 25736881]
62. Lovley DR & Holmes DE Electromicrobiology: the ecophysiology of phylogenetically diverse electroactive microorganisms. *Nature reviews*. Microbiology 20, 5–19 (2022). [PubMed: 34316046]
63. Lovley DR & Yao J Intrinsically Conductive Microbial Nanowires for 'Green' Electronics with Novel Functions. Trends Biotechnol 39, 940–952 (2021). [PubMed: 33419586]
64. Lovley DR & Holmes DE Protein Nanowires: the Electrification of the Microbial World and Maybe Our Own. J Bacteriol 202(2020).
65. Bray MS et al. Phylogenetic and structural diversity of aromatically dense pili from environmental metagenomes. Environmental Microbiology Reports 12, 49–57 (2020). [PubMed: 31701641]
66. Craig L et al. Type IV pilus structure by cryo-electron microscopy and crystallography: implications for pilus assembly and functions. Molecular Cell 23, 651–662 (2006). [PubMed: 16949362]
67. Bardiaux B et al. Structure and Assembly of the Enterohemorrhagic Escherichia coli Type 4 Pilus. Structure 27, 1082–1093 e5 (2019). [PubMed: 31056419]
68. Lopez-Castilla A et al. Structure of the calcium-dependent type 2 secretion pseudopilus. Nat Microbiol 2, 1686–1695 (2017). [PubMed: 28993624]
69. Neuhaus A et al. Cryo-electron microscopy reveals two distinct type IV pili assembled by the same bacterium. Nat. Commun. 11, 2231 (2020). [PubMed: 32376942]
70. Cosert KM, Castro-Forero A, Steidl RJ, Worden RM & Reguera G Bottom-up fabrication of protein nanowires via controlled self-assembly of recombinant Geobacter pilins. mBio 10(2019).

71. Devaraj A et al. The extracellular DNA lattice of bacterial biofilms is structurally related to Holliday junction recombination intermediates. Proc. Natl. Acad. Sci. U.S.A. 116, 25068–25077 (2019). [PubMed: 31767757]
72. Slinker JD, Muren NB, Renfrew SE & Barton JK DNA charge transport over 34 nm. Nat Chem 3, 228–33 (2011). [PubMed: 21336329]
73. Butler JE, Young ND, Aklujkar M & Lovley DR Comparative genomic analysis of *Geobacter sulfurreducens* KN400, a strain with enhanced capacity for extracellular electron transfer and electricity production. BMC Genomics 13, 471 (2012). [PubMed: 22967216]
74. Edwards MJ, White GF, Butt JN, Richardson DJ & Clarke TA The Crystal Structure of a Biological Insulated Transmembrane Molecular Wire. Cell 181, 665–673.e10 (2020). [PubMed: 32289252]
75. Li DB et al. His/Met heme ligation in the PioA outer membrane cytochrome enabling light-driven extracellular electron transfer by Rhodopseudomonas palustris TIE-1. Nanotechnology 31, 354002 (2020). [PubMed: 32403091]
76. Jiang X et al. Which multi-heme protein complex transfers electrons more efficiently? Comparing MtrCAB from *Shewanella* with OmcS from *Geobacter*. Journal of Physical Chemistry Letters 11, 9421–9425 (2020). [PubMed: 33104365]
77. Wang F et al. An extensively glycosylated archaeal pilus survives extreme conditions. Nat Microbiol 4, 1401–1410 (2019). [PubMed: 31110358]
78. Huerta-Miranda GA, Arroyo-Escoto AI, Burgos X, Juarez K & Miranda-Hernandez M Influence of the major pilA transcriptional regulator in electrochemical responses of *Geobacter sulfureducens* PilR-deficient mutant biofilm formed on FTO electrodes. Bioelectrochemistry 127, 145–153 (2019). [PubMed: 30825658]
79. Malvankar NS, Yalcin SE, Tuominen MT & Lovley DR Visualization of charge propagation along individual pili proteins using ambient electrostatic force microscopy. Nat. Nanotechnol. 9, 1012–7 (2014). [PubMed: 25326694]
80. Ing NL, Nusca TD & Hochbaum AI *Geobacter sulfurreducens* pili support ohmic electronic conduction in aqueous solution. Phys Chem Chem Phys 19, 21791–21799 (2017). [PubMed: 28783184]
81. De Carlo S & Harris JR Negative staining and cryo-negative staining of macromolecules and viruses for TEM. Micron 42, 117–131 (2011). [PubMed: 20634082]
82. Kemp AD, Harding CC, Cabral WA, Marini JC & Wallace JM Effects of tissue hydration on nanoscale structural morphology and mechanics of individual Type I collagen fibrils in the Brtl mouse model of Osteogenesis Imperfecta. J. Struct. Biol. 180, 428–38 (2012). [PubMed: 23041293]
83. Jesior JC & Wade RH Electron-irradiation-induced flattening of negatively stained 2D protein crystals. Ultramicroscopy 21, 313–9 (1987). [PubMed: 3629735]
84. Xu S & Arnsdorf MF Scanning (atomic) force microscopy imaging of earthworm haemoglobin calibrated with spherical colloidal gold particles. J Microsc 187, 43–53 (1997). [PubMed: 9263439]
85. Chan CH, Levar CE, Zacharoff L, Badalamenti JP & Bond DR Scarless genome editing and stable inducible expression vectors for *Geobacter sulfurreducens*. Appl. Environ. Microbiol. 81, 7178–7186 (2015). [PubMed: 26253675]
86. Damron FH et al. Construction of mobilizable mini-Tn7 vectors for bioluminescent detection of gram-negative bacteria and single-copy promoter lux reporter analysis. Appl Environ Microbiol 79, 4149–53 (2013). [PubMed: 23584769]
87. Zacharoff L, Chan CH & Bond DR Reduction of low potential electron acceptors requires the CbcL inner membrane cytochrome of *Geobacter sulfurreducens*. Bioelectrochemistry (Amsterdam, Netherlands) 107, 7–13 (2016).
88. Marsili E, Rollefson JB, Baron DB, Hozalski RM & Bond DR Microbial biofilm voltammetry: direct electrochemical characterization of catalytic electrode-attached biofilms. Appl Environ Microbiol 74, 7329–37 (2008). [PubMed: 18849456]
89. Schagger H Tricine-SDS-PAGE. Nat Protoc 1, 16–22 (2006). [PubMed: 17406207]

90. Kavran JM & Leahy DJ Silver staining of SDS-polyacrylamide gel. Meth. Enzymol. 541, 169–76 (2014).
91. Thomas PE, Ryan D & Levin W An improved staining procedure for the detection of the peroxidase activity of cytochrome P-450 on sodium dodecyl sulfate polyacrylamide gels. Anal Biochem 75, 168–76 (1976). [PubMed: 822747]
92. Strohalm M, Kavan D, Novak P, Volny M & Havlicek V mMass 3: a cross-platform software environment for precise analysis of mass spectrometric data. Anal Chem 82, 4648–51 (2010). [PubMed: 20465224]
93. Strohalm M, Hassman M, Kosata B & Kodicek M mMass data miner: an open source alternative for mass spectrometric data analysis. Rapid Commun Mass Spectrom 22, 905–8 (2008). [PubMed: 18293430]
94. Niedermeyer TH & Strohalm M mMass as a software tool for the annotation of cyclic peptide tandem mass spectra. (2012).
95. Rohou A & Grigorieff N CTFFIND4: Fast and accurate defocus estimation from electron micrographs. J. Struct. Biol. 192, 216–21 (2015). [PubMed: 26278980]
96. Punjani A, Rubinstein JL, Fleet DJ & Brubaker MA cryoSPARC: algorithms for rapid unsupervised cryo-EM structure determination. Nat. Methods 14, 290–296 (2017). [PubMed: 28165473]
97. Zheng SQ et al. MotionCor2: anisotropic correction of beam-induced motion for improved cryo-electron microscopy. Nat. Methods 14, 331–332 (2017). [PubMed: 28250466]
98. Egelman EH A robust algorithm for the reconstruction of helical filaments using single-particle methods. Ultramicroscopy 85, 225–34 (2000). [PubMed: 11125866]
99. Egelman EH Reconstruction of helical filaments and tubes. Methods Enzymol 482, 167–83 (2010). [PubMed: 20888961]
100. Afonine PV et al. New tools for the analysis and validation of cryo-EM maps and atomic models. Acta Crystallogr D Struct Biol 74, 814–840 (2018). [PubMed: 30198894]
101. Pettersen EF et al. UCSF Chimera--a visualization system for exploratory research and analysis. J Comput Chem 25, 1605–12 (2004). [PubMed: 15264254]
102. Afonine PV et al. Real-space refinement in PHENIX for cryo-EM and crystallography. Acta Crystallogr D Struct Biol 74, 531–544 (2018). [PubMed: 29872004]
103. Williams CJ et al. MolProbity: More and better reference data for improved all-atom structure validation. Protein Science 27, 293–315 (2018). [PubMed: 29067766]
104. Clarke TA, Cole JA, Richardson DJ & Hemmings AM The crystal structure of the pentahaem c-type cytochrome NrfB and characterization of its solution-state interaction with the pentahaem nitrite reductase NrfA. Biochem J 406, 19–30 (2007). [PubMed: 17521287]
105. Rodrigues ML, Oliveira TF, Pereira IA & Archer M X-ray structure of the membrane-bound cytochrome c quinol dehydrogenase NrfH reveals novel haem coordination. EMBO J 25, 5951–60 (2006). [PubMed: 17139260]
106. Pettersen EF et al. UCSF ChimeraX: Structure visualization for researchers, educators, and developers. Protein Sci 30, 70–82 (2021). [PubMed: 32881101]

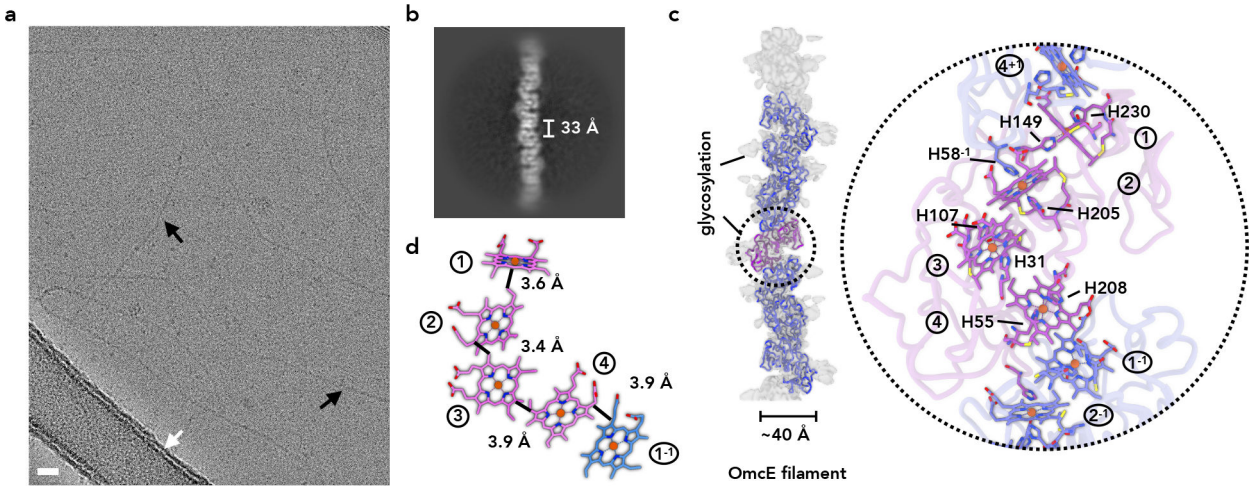

Figure 1. Cryo-EM of OmcE filaments.

(a) Representative cryo-EM image of the purified OmcE filaments (black arrow) from the OmcS-H357M producing variant strain of *G. sulfurreducens*, taken from the 35,976 images recorded. Lacey carbon grids were used for the cryo-EM imaging (carbon film indicated by white arrow). The sample was treated with DNase I prior to freezing. Scale bar, 200 Å.

(b) A two-dimensional class average of the OmcE filament, showing the rise of 34 Å between adjacent subunits.

(c) The surface of the reconstruction (transparent gray) with backbone trace of the OmcE subunits. A zoomed region of the circle is shown on the right: the hemes and their coordinating histidines are labeled.

(c) The heme array in OmcE, with the minimum observed edge-to-edge distances indicated between adjacent hemes. The heme from the adjacent subunit is shown in blue.

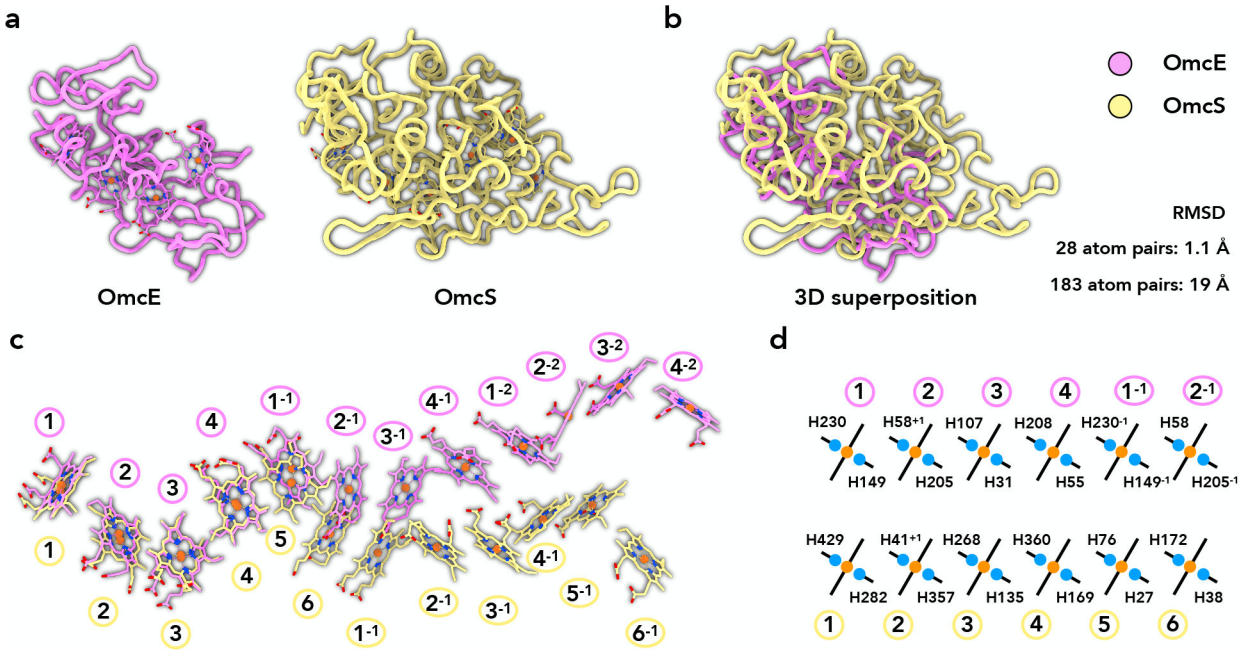

Figure 2. OmcE versus OmcS, very different protein structures but almost identical heme packing

(a) The backbone traces of single OmcE and OmcS subunits. The heme molecules are shown as sticks.

(b) Alignment of OmcE and OmcS proteins. The RMSD of the aligned atom pairs and total atom pairs are shown.

(c) The comparison of heme chains in OmcE and OmcS filaments. The OmcS filament is aligned to the OmcE subunit on the left containing hemes 1–4.

(d) The bis-histidine coordinations for the six hemes aligned in (c). The iron atoms in heme are shown as orange circles, and the imidazole side chains of the histidines are represented with blue circles.

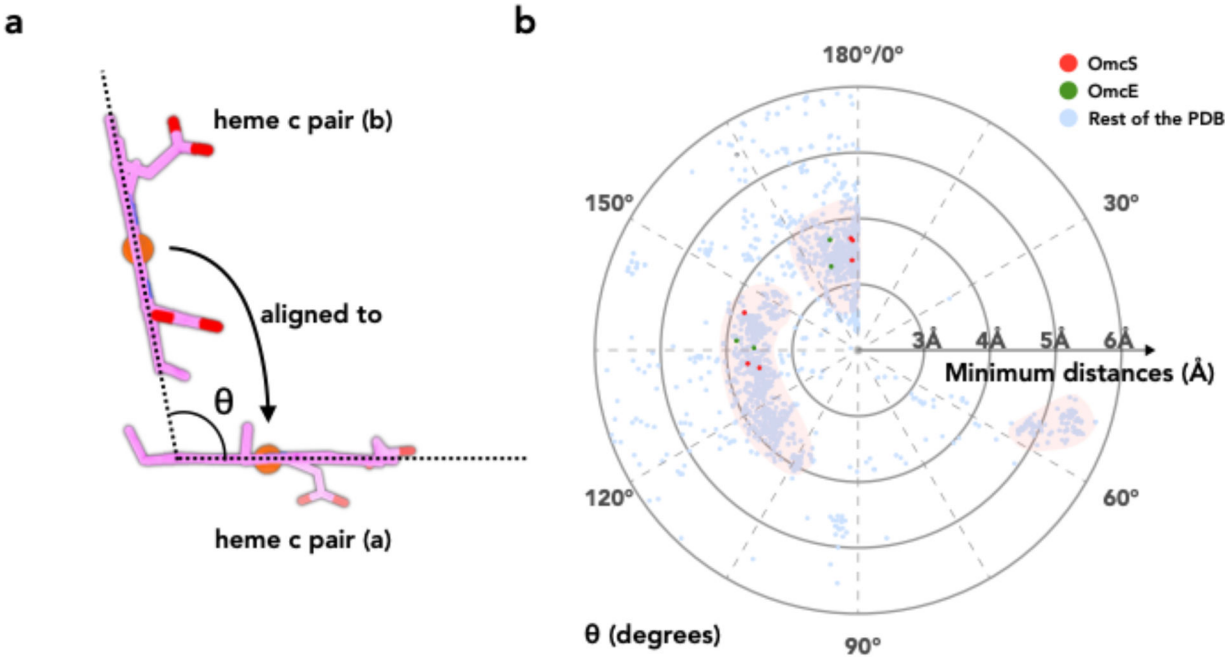

Figure 3. Orientation plot for heme-c pairs

(a) One heme in a pair can be aligned to the other heme by a rotation and a translation. The rotation angle θ is shown. For example, as shown in Fig. 2c, the rotation angle θ between heme 1 and heme 2 is ~130°, between heme 2 and heme 3 is ~175°, and between heme 3 and heme 4 is ~140°.

(b) The heme (heme c only, ligand ID: HEC) pairs in all PDB structures were analyzed. The minimum distances refer to the smallest distance between the heme pairs, regardless of the atom type. The angle θ was determined from the alignment rotation matrix between heme pairs. For example, θ=0° means two hemes are perfectly parallel, while θ=180° means two hemes are perfectly antiparallel (flipped) during the alignment. All heme pairs with a minimum distance less than or equal to 6 Å are shown. The heme pairs in the OmcE and OmcS filaments are highlighted in green and red, respectively.

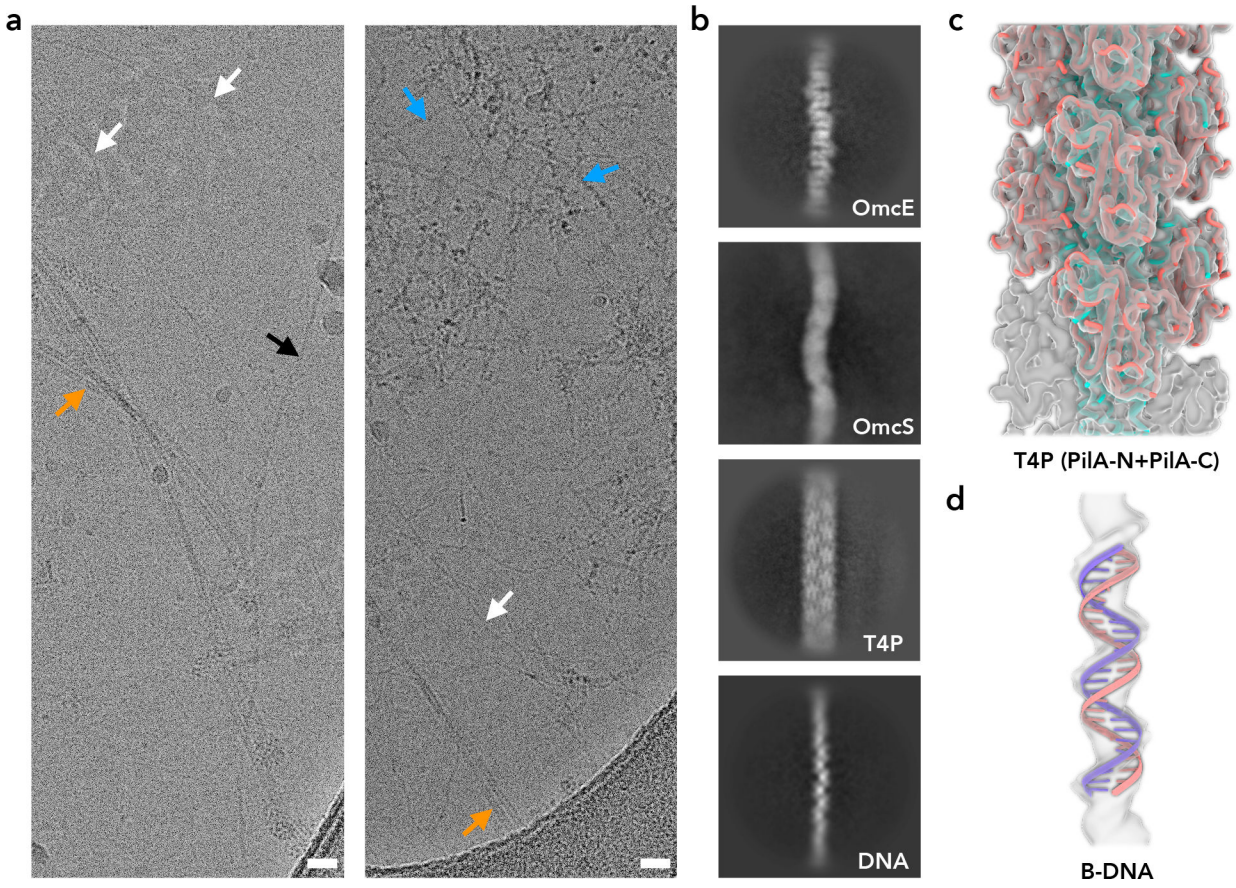

Figure 4. Mixtures of OmcS variant (H357M), extracellular T4P, DNA, and OmcE filaments

(a) Representative cryo-EM image of filaments sheared and precipitated from an overproducing OmcS-H357M variant strain of *G. sulfurreducens*, taken from the 17,105 images recorded. The sample was not treated with DNase I prior to freezing, and was not centrifuged to remove aggregates as in Fig. 1. Other than OmcS filaments, other species of filaments were observed and labeled correspondingly: OmcE filaments (black arrow), OmcS filaments (blue arrows), PilA-N-C type IV pili (orange arrows), and extracellular B-form DNA (white arrows). Scale bar, 200 Å.

(b) Two-dimensional averages of the four different filaments in (a), showing that these different filaments are easily distinguishable.

(c) A ~4.1 Å cryo-EM reconstruction of the Type IV pili, with ribbon model of the PilA subunits containing two chains, PilA-N (cyan) and PilA-C (orange).

(d) A ~10 Å cryo-EM reconstruction of DNA filaments showing a clear pitch of ~ 36 Å with ribbon model of B-DNA.